Far-field imaging of acoustic waves by a two-dimensional sonic crystal

Chunyin Qiu,[1] Xiangdong Zhang,[2] and Zhengyou Liu[1,*]
[1]*Deparment of Physics, Wuhan University, Wuhan 430072, People's Republic of China*
[2]*Deparment of Physics, Beijing Normal University, Beijing 100875, People's Republic of China*
(Received 5 September 2004; published 10 February 2005)

The negative refraction behavior and imaging effect for acoustic waves in two-dimensional sonic crystals consisting of hexagonal arrays of steel cylinders in air are studied in this paper. The negative refraction and left-handed behaviors are demonstrated by the simulation of a Gaussian beam through a slab of the sonic crystal. Imaging effects by the sonic crystal slab with effective refraction index $n \neq -1$ and $n=-1$ are investigated, respectively. Far-field images by two-dimensional sonic-crystal-based superlens for both cases are obtained by exact numerical simulations, which is in agreement with the physical analysis based on the wave-beam negative refraction law. Thus, extensive applications of such a phenomenon to acoustic devices are anticipated.

DOI: 10.1103/PhysRevB.71.054302 PACS number(s): 78.20.Ci, 43.20.+g, 43.58.+z

I. INTRODUCTION

During the past few years, there has been a great deal of interest in studying a novel class of media that has become known as the left-handed materials.[1–10] These materials are characterized by simultaneous negative permittivity and permeability. Properties of such materials were analyzed theoretically by Veselago over 30 years ago,[1] but only recently were they demonstrated experimentally.[4,5] As was shown by Veselago, the left-handed materials possess a number of unusual electromagnetic effects including negative refraction index,[1] inverse Snell's law,[7,8] reversed Doppler shift,[9] and reversed Cerenkov radiation.[10] These anomalous features allow considerable control over light propagation and open the door for new approaches to a variety of applications. For example, the negative refraction effect makes it possible to image with a flat lens. Recently, the similar negative refraction behavior and/or imaging effect has also been found in photonic crystals.[11–14] Such a photonic crystal behaves as a material having an effective refractive index (ERI) controllable by the band structure. In these photonic crystals, there are two kinds of cases for negative refraction occurring. The first is the left-handed behavior described as above.[12] In this case, $\vec{k}$, $\vec{E}$, and $\vec{H}$ form a left-handed set of vectors, i.e., $\vec{S}\cdot\vec{k}<0$, where $\vec{S}$ is the Pointing vectors. Another case is due to the negative-definite photonic effective mass.[13,14] That is to say, the negative refraction can be realized without employing a negative index or a backward wave effect. In this case, the photonic crystal is behaving very similar to a uniform right-handed medium, i.e., $\vec{S}\cdot\vec{k}>0$. Therefore, the photonic crystal represents another class of materials with electromagnetic properties not available in a conventional medium.

In analogy with negative-refraction behavior of electromagnetic wave in photonic crystal, the phenomena of negative-refraction for the other classical waves had also been investigated recently. Negative-refraction and imaging effects of water surface wave by a periodic structure were theoretically and experimentally demonstrated recently.[15] Our recent work also exhibits that the negative-refraction behavior and imaging effect for acoustic wave can be observed in the sonic crystal consisting of a square array of rigid or liquid cylinders embedded in an air background.[16] Both of the observations, for water surface wave and acoustic wave, were realized at the lowest valence band with $\vec{S}\cdot\vec{k}>0$, thus without employing a left-handed behavior or a backward wave effect.

The advantages of the negative refraction in the lowest valence band are single-mode and high transmission. These can help us to design microsuperlens and realize the focusing of the wave. Recently, the subwavelength focusing and image of electromagnetic wave by two-dimensional photonic crystal slab have been observed experimentally.[14,17,18] However, due to the anisotropy of dispersion for the lowest valence band in two-dimensional photonic crystal with square lattice, such images only appear in near-field region.[13,19] Thus, extensive applications of such a phenomenon are limited. Very recent research shows[20] that all-angle single-beam left-handed behaviors for both polarized electromagnetic wave exist in the two-dimensional coated photonic crystals with triangular lattice. Good-quality non-near-field images and focusing have been observed in these systems for the electromagnetic waves. Motivated by these works, in this paper, we investigate the far-field focusing and imaging of acoustic waves in sonic crystals of steel cylinders surrounded by air. The existence of band gaps in such systems was confirmed by theory and experiment.[21,22] For the sake of tractability, throughout the paper we adopt the multiple scattering theory (MST) method[23,24] as our main computational tool, both to calculate the photonic band structure in the reciprocal space and to perform numerical simulations for wave propagating in the finite real space. The detailed description of this method has been given in Refs. 23 and 24.

This paper is organized as follows. In Sec. II, we analyze and simulate the negative-refraction behavior for acoustic waves through a slab of sonic crystal consisting of a hexagonal array of steel cylinders in air background. In Sec. III imaging effects for the sonic crystals with the ERI $n=-0.7$ and $n=-1$ are both simulated and discussed in detail. A brief summary is given in Sec. IV.

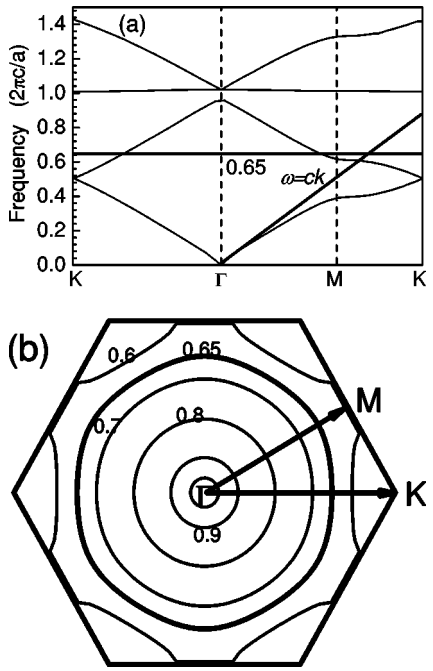

FIG. 1. (a) Band structure for the sonic crystal consisting of steel cylinders in air background arranged in a hexagonal lattice, with a filling ratio 0.47. The straight line beginning at point Γ represents the dispersion relation of air, i.e., $\omega=ck$, and the horizontal line marks the frequency 0.65. (b) EFCs for some frequencies at the second band, moving inwards with increasing frequencies.

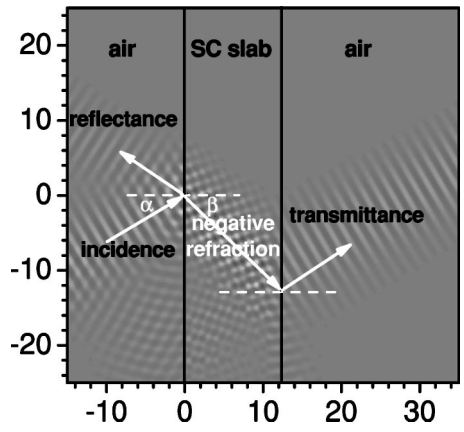

FIG. 2. Pressure field patterns generated by an incident Gaussian beam on a nine-layer sample. Light and dark regions denote positive and negative pressures, respectively, and the vertical black lines mark the sample surfaces. The propagation directions of the Gaussian beam are marked by arrows, with α and β denoting the incident and refractive angles. The scale is in unit of a, the lattice constant.

II. THE NEGATIVE REFRACTION AND LEFT-HANDED BEHAVIOR OF ACOUSTIC WAVE IN SONIC CRYSTAL

We consider a sonic crystal consisting of a hexagonal array of steel cylinders in air background, with a filling ratio 0.47. Many works[11–14,17–20] had demonstrated that negative refraction in photonic crystal could be deduced by studying the equifrequency surfaces (EFS) of band structures. Similarly, an understanding of negative-refraction behavior for acoustic wave in a sonic crystal can be achieved by examining the band structure and EFS of the sonic crystal. Figures 1(a) and 1(b) show the band structure and some EFS for the sonic crystal respectively, which are calculated by the MST approach.[23] The material parameters used in the calculations are density $\rho=1.29$ g/m^3 and sound velocity $c=340$ m/s for air, and density $\rho=7.67$ g/cm^3, longitudinal wave velocity $c_l=6010$ m/s and transverse wave velocity $c_t=3230$ m/s for steel. For comparison, in Fig. 1(a), we also depict the dispersion curve for air, which is the straight line beginning at Γ point. The horizontal line in Fig. 1(a) delineates frequency 0.65 (in unit of $2\pi c/a$, where a is the lattice constant), and Fig. 1(b) shows the EFS for frequency 0.65 and some other frequencies nearby. From Figs. 1(a) and 1(b) we can infer that the negative-refraction behavior can occur at the second band because the EFS move inwards with increasing frequencies.[12] It's easy to know that $\vec{S}\cdot\vec{k}<0$ in this case. In Fig. 1(b), we note that the EFS have different shapes, but within frequency range 0.65–0.95, the EFS are close to circles. Thus in this frequency range, there exists well-defined effective refractive index (ERI) for the sonic crystal, which is $n=-|\overline{k}|c/\omega$.

In order to study the refractive behavior of acoustic waves occurring at the interface of the sonic crystal and background medium, an efficient finite system MST approach[24] is employed to calculate the pressure field generated by a Gaussian beam[25] incident onto a sonic crystal slab. In the simulation, a nine-layer sample is used, and the normal of the sample surface is chosen along ΓM direction (hereafter, ΓM direction is implied throughout this paper). The incident Gaussian beam used in simulation has a frequency 0.65(corresponding to a wavelength of $\lambda\approx1.54a$) and an incidence angle $\alpha=30°$. For this frequency, the sonic crystal has an ERI $n\approx-0.7$, the expected refraction angle should be $\arcsin(\sin\alpha/n)\approx45°$, according to the Snell's law. With the simulation result shown in Fig. 2, it can be found that at both of the interfaces, there exhibit the obvious negative refraction behaviors. The refractive angle can be evaluated as $\beta\approx-43°$, very close to above prediction. Varying the incident angle of the Gaussian beam, we have checked the cases with various incident angles. When the incident angle is smaller than the Brewster angle $[\arcsin(0.7)\approx44°]$, all-angle negative refractions have been demonstrated at this case. This can help us to design the superlens for an acoustic wave.

III. THE IMAGING EFFECT OF ACOUSTIC WAVE BY A SONIC CRYSTAL SLAB

We now turn to the investigation of the imaging effect and superlens of acoustic wave based on the above sonic crystal. We have known in preceding section that this sonic crystal can be described by a negative ERI $n\approx-0.7$ at frequency 0.65, so it would be helpful for us to first analyze how acoustic waves propagate through a slab of the material with negative ERI via a simple ray-trace picture. Figure 3 shows such

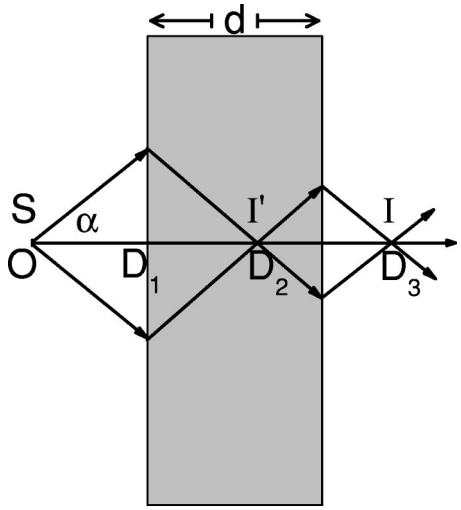

FIG. 3. A "ray-trace" schematic picture governed by wave-beam refraction law.

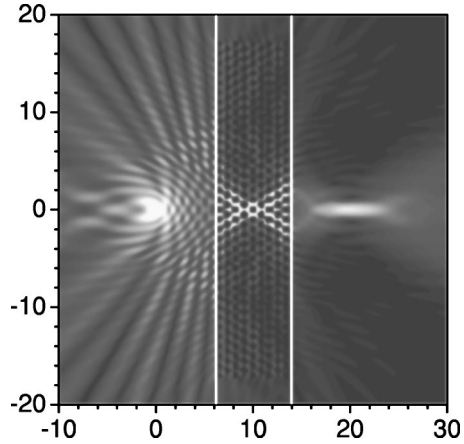

FIG. 4. The intensity distributions of pressure field of a point source and its image across a nine-layer sample, with $D_1=6a$. Lightness and darkness denote strong and weak intensity distributions of pressure field, respectively. The vertical lines mark the sample surfaces.

a slab, which has a negative ERI n and a thickness d placed in a positive refraction index material background (with $n=1$). A point source S is placed on the left side of the slab, with a distance D_1 from the left side surface. From the "ray-trace" analysis we know that the two rays radiated from the source with incident angle α, as schematically shown in Fig. 3, will meet inside the slab at I' first and meet again across the slab at I on the right side. The distances of I' and I from S can be obtained, respectively, as

$$D_2 = (1 + \sqrt{n^2 - \sin^2 \alpha}/\cos \alpha)D_1 \tag{1}$$

and

$$D_3 = (1 + \cos \alpha/\sqrt{n^2 - \sin^2 \alpha})d. \tag{2}$$

Obviously, D_2 and D_3 depend on α if $n \neq -1$, which means that the rays radiated from the source with different incident angles can not be focused into a single point. There is a linear relation between D_2 and D_1 (independent on the slab thickness d), and a linear relation between D_3 and d (independent on source-slab distance D_1). In contrast, if $n=-1$, D_2 and D_3 will not depend on α any longer, all the rays radiated from the source could be focused on I' inside the slab and focused again on I across the slab, with

$$D_2 = 2D_1 \tag{3}$$

and

$$D_3 = 2d. \tag{4}$$

The points I' and I are two images of the source S, we expect they are of high quality, because they are the foci of all rays from the source. We term the focusing corresponding to $n=-1$ as "ideal imaging" hereafter in order to distinguish from the imaging effect corresponding to $n \neq -1$ as described above.

As described above, for a slab of sonic crystal with ERI $n \approx -0.7$, we cannot expect to observe an ideal imaging effect. However, because only the rays with incident angle smaller than 44° [which is the Brewster angle, $\arcsin(0.7) \approx 44°$] radiated from the source can refract into the sample (other rays with angle larger than 44° are totally reflected by the sample), a near-axis approximation might be roughly applied such that

$$D_2 = (1 + |n|)D_1 \tag{5}$$

and

$$D_3 = (1 + 1/|n|)d, \tag{6}$$

which become incident angle independent now. We might thus be able to observe an imaging effect by this sonic crystal slab. For a slab of the sonic crystal with hexagonal structure, the effective thickness of the slab d can be estimated as the maximum distance between the two surfaces of sample, i.e.,

$$d = \frac{\sqrt{3}}{2}(l-1)a + 2r, \tag{7}$$

with r being the radius of the cylinder and l being the layer number of slab. In order to verify this conjecture, we perform a MST simulation for a nine-layer sample of the sonic crystal. A point source is placed on the left side of the sample with a distance $6a$ from the sample's left surface (i.e., source-slab distance $D_1=6a$). With the intensity distributions of pressure field plotted in Fig. 4, obvious focusing effects can be observed both inside and outside the sample, with foci centers at $10.1a$ and $19.3a$ (measured from the point source), respectively. Since the thickness of the sample is $d=7.76a$, D_2 and D_3 can be estimated from Eqs. (5) and (6) as $10.2a$ and $18.8a$, which are very close to above simulation results. Compared with the image of a point source formed by a slab of the sonic crystal having a square array,[16] the image observed here has a comparatively big separation from the right surface of the sample; it is in fact a far-field image.

Fixing the source-slab distance $D_1=6a$, we perform a further simulation for a new sample of 15 layers; the results are shown in Fig. 5(a). We find that the foci center inside the

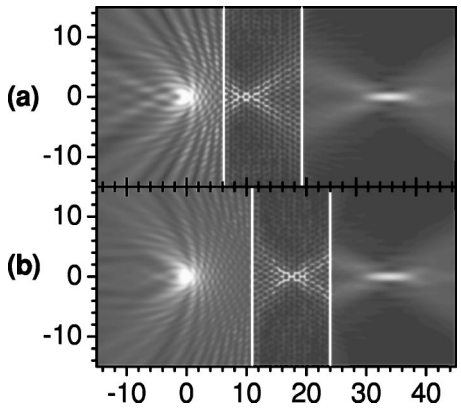

FIG. 5. The intensity distributions of pressure field of a point source and its image across a 15-layer sample, with (a) $D_1=6a$ and (b) $D_1=11a$, respectively. Lightness and darkness denote strong and weak intensity distributions of pressure field, respectively. The vertical lines mark the sample surfaces.

slab is still at around $10.2a$, which confirms the independence of D_2 on d. But the foci center outside the sample moves rightwards to $33.8a$, close to the prediction from Eq. (6): $31.5a$. An additional simulation for this 15-layer sample is performed by increasing the source-slab distance to $D_1=11a$ and the simulation result is shown in Fig. 5(b). It is now observed that the foci center inside the sample moves rightwards to $18.5a$, close to the predicted position $18.7a$, but the foci center outside the sample keeps almost unchanged at $33.8a$, which verifies that D_3 is independent of D_1.

Although it has shown that slabs of the sonic crystal consisting of a hexagonal array of steel cylinders in air with the filling ratio 0.47 (at frequency 0.65, the crystal has ERI −0.7) can work as superlens and form far-field images across the slabs, however, as we observed, all of the images are elongated in the axial direction compared with the point source. We can understand that the distortion of the images comes from the mismatch of the refraction index of the sonic crystal slab with that of the surrounding medium. For this reason, looking for a sonic crystal which possesses an ERI $n\approx-1$ becomes very important to achieve ideal imaging by a flat slab of the sonic crystal by taking advantage of negative refraction phenomena. By analyzing the band structure varying with the filling ratio, one can find that increasing the filling ratio of the sonic crystal can flatten the second band, which is helpful to get a round EFS and achieve ERI $n\approx-1$. Such EFSs are indeed obtained when the filling ratio is increased to an extremely high value, 0.906, at which the steel cylinder inclusions in the crystal are almost close-packed. From the band structure and some EFS at the second band shown in Figs. 6(a) and 6(b), we can observe that the EFSs are approximately circular within the frequency range 0.355–0.410, thus there exists isotropic negative ERI for the sonic crystal in the frequency range, as shown in Fig. 7. The ERI $n=-1$ can be achieved at frequency around 0.365 (corresponding to a wavelength of $\lambda=2.74a$), which is stressed by the horizontal line in Fig. 6(a) and by the thick circle in Fig. 6(b).

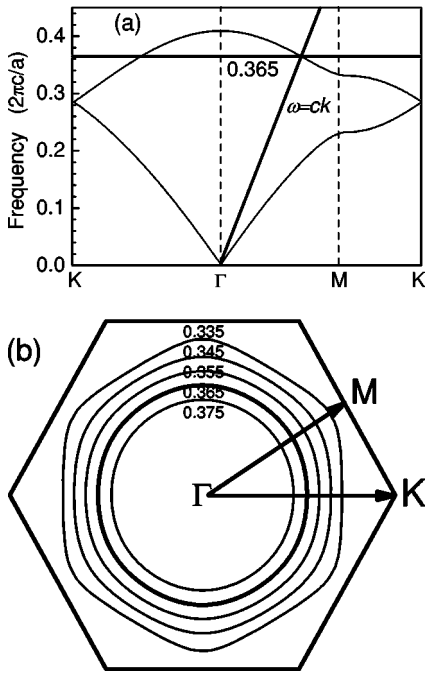

FIG. 6. (a) Band structure for the sonic crystal consisting of steel cylinders in air background arranged in a hexagonal lattice, with a filling ratio 0.906. The straight line beginning at point Γ represents dispersion relation of air $\omega=ck$, and the horizontal line denotes frequency 0.365. (b) EFCs for some frequencies at the second band, moving inwards with increasing frequencies.

In order to test the above analysis, similar simulations for some samples of the sonic crystal are performed. The first simulation is for a six-layer sample, with the source-slab distance $D_1=3.5a$. As shown in Fig. 8(a), we see that the acoustic waves radiated from the point source on the left side (source side) of the sample, transmit through the sample and focus onto an ideal image on the right side (image side) finally, with a distance of $10.8a$ from the source (i.e., source-image distance $D_3=10.8a$). It should be noted that since the pressure field on the image side is only 10% of the source side, to make the figure more readable, the pressure field on the image side has been amplified ten times on purpose. One may find that the image is in phase with the point source (*both the pressure fields are positive*), which is easy to understand from the "ray-trace" picture shown in Fig. 3, the phase increase for a ray in the positive refractive index back-

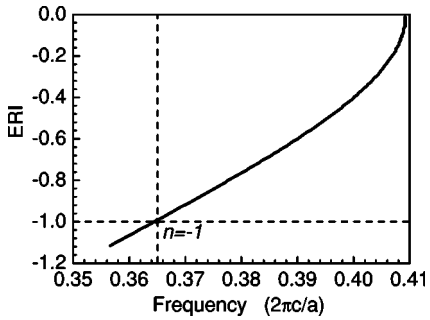

FIG. 7. The isotropic negative ERI n vs frequency.

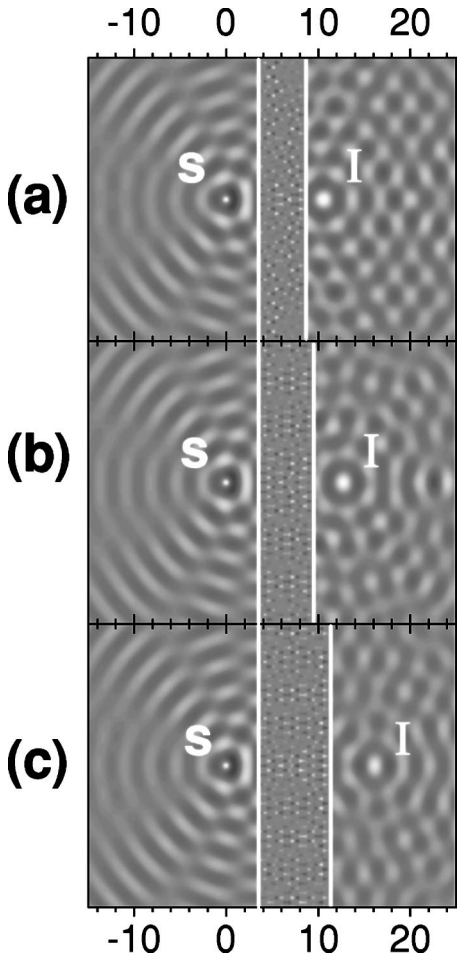

FIG. 8. Pressure patterns of a point source and its image across (a) six-layer, (b) seven-layer, and (c) nine-layer samples, respectively, with $D_1=3.5a$ kept fixed. Light and dark regions denote positive and negative pressure fields, respectively.

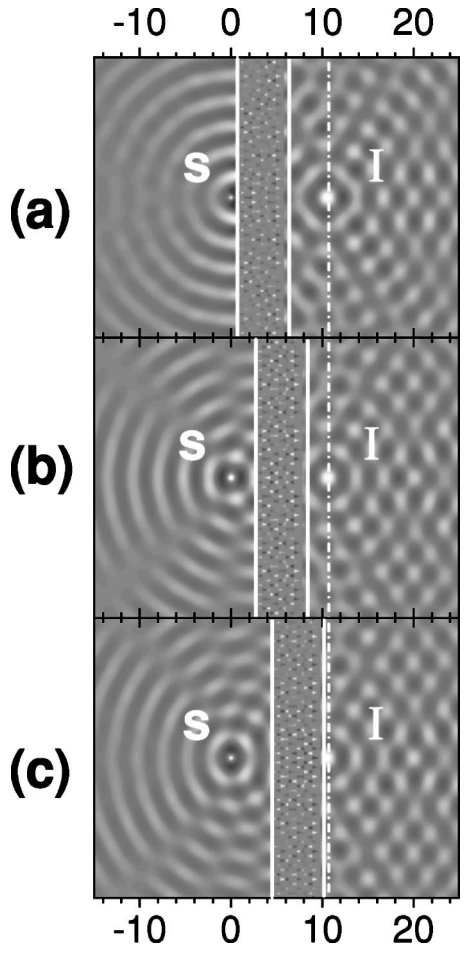

FIG. 9. Pressure patterns of a point source and its image across a 6-layer sample, with (a) $D_1=0.5a$, (b) $D_1=2.5a$ and (c) $D_1=4.5a$, respectively. Light and dark regions denote positive and negative pressure fields, respectively.

ground medium, i.e., the air, is right compensated by the same amount of decrease in the negative refractive index slab, i.e., the sample, since the slab has a refractive index of $n=-1$ (in order to stress the phase relations between the point source and the image, all the simulations hereafter will be displayed with the pressure field patterns instead of the intensity patterns). One can also note that the images inside the samples, as observed in the case with $n\approx-0.7$, are not visible in the present case. The reason is that, since the acoustic waves can hardly penetrate into the steel cylinders owing to the big mismatch between the steel cylinders and the air, while the steel cylinders are almost close packed, there remain very small and quite separated interstitial air areas in the crystal to contain the waves, which is too difficult to construct a visible image.

For $n=-1$, we have known that the source-image distance $D_3=2d$. The thickness for the six-layer sample is $d=5.33a$, while the simulation gives $D_3=10.8a$, we see $D_3=2d$ is indeed satisfied. To further verify this relation, two additional simulations for a seven-layer sample and a nine-layer sample are performed. From Figs. 8(b) and 8(c), we find that the image moves rightwards to $12.5a$ for the seven-layer sample, and to $16.1a$ for the nine-layer sample, respectively. Since the thicknesses for these two samples can be evaluated to be $d=6.20a$ and $7.93a$, respectively, we see again $D_3=2d$ is satisfied. To verify the independence of source-image distance D_3 on source-slab distance D_1, we perform three further simulations for the six-layer sample, by setting $D_1=0.5a$, $2.5a$ and $4.5a$, respectively. Figures 9(a)–9(c) show the simulation results, and one can note that although D_1 changes from $0.5a$ to $2.5a$ and then to $4.5a$, the source-image distance keeps at $10.8a$ without any change, which verify the independence of D_3 on D_1.

IV. CONCLUSION

Based on the exact numerical simulations and physical analysis, we have studied the negative refraction behavior and imaging effect for acoustic waves in two-dimensional sonic crystals consisting of hexagonal arrays of steel cylinders in air. The negative refraction and left-handed behaviors have been demonstrated by the simulation of a Gaussian beam through a slab of the sonic crystal. Imaging effects by the sonic crystal slab with effective refraction index $n\neq-1$

and $n=-1$ have been investigated, respectively. The far-field images by two-dimensional sonic-crystal-based superlens for both cases have been obtained by the exact numerical simulations, which is in agreement with the physical analysis based on the wave-beam negative refraction law. The far-field imaging effect for acoustic waves in sonic crystals may have important applications in the ultrasonic device designing. Thus, extensive applications of such a phenomenon to acoustic devices are anticipated.

ACKNOWLEDGMENTS

This work was supported by the National Natural Science Foundation of China (Grant Nos. 50425206, 10174054, and 10374009) and Doctoral Research Foundation of Ministry of Education of China (Grant No. 20020486013). X. Z would like to thank the National Key Basic Research Special Foundation of China under Grant No.2001CB610402 and the Grant from Beijing Normal University.

*Electronic address: zyliu@whu.edu.cn

[1] V. G. Veselago, Sov. Phys. Usp. **8**, 2854 (1967) [Sov. Phys. Usp. **10**, 509 (1968)].
[2] J. B. Pendry, A. J. Holden, D. J. Robbins, and W. J. Stewart, IEEE Trans. Microwave Theory Tech. **47**, 2075 (1999).
[3] J. B. Pendry, Phys. Rev. Lett. **85**, 3966 (2000).
[4] D. R. Smith, W. J. Padilla, D. C. Vier, S. C. Nemat-Nasser, and S. Schultz, Phys. Rev. Lett. **84**, 4184 (2000).
[5] R. A. Shelby, D. R. Smith, and S. Schultz, Science **292**, 77 (2001).
[6] P. Markos and C. M. Soukoulis, Phys. Rev. E **65**, 036622 (2002); Phys. Rev. B **65**, 033401 (2002).
[7] S. Foteinopoulou, E. N. Economou, and C. M. Soukoulis, Phys. Rev. Lett. **90**, 107402 (2003).
[8] A. A. Houck, J. B. Brock, and I. L. Chuang, Phys. Rev. Lett. **90**, 137401 (2003).
[9] E. J. Reed, M. Soljacic, and J. D. Joannopoulos, Phys. Rev. Lett. **91**, 133901 (2003).
[10] C. Luo, M. Ibanescu, S. G. Johnson, and J. D. Joannopoulos, Science **299**, 368 (2003).
[11] H. Kosaka, T. Kawashima, A. Tomita, M. Notomi, T. Tamamura, T. Sato, and S. Kawakami, Phys. Rev. B **58**, R10 096 (1998).
[12] M. Notomi, Phys. Rev. B **62**, 10 696 (2000).
[13] C. Luo, S. G. Johnson, J. D. Joannopoulos, and J. B. Pendry, Phys. Rev. B **65**, 201104(R) (2002); **68**, 045115 (2003).
[14] E. Cubukcu, K. Aydin, E. Ozbay, S. Foteinopoulou, and C. M. Soukoulis, Nature (London) **423**, 604 (2003).
[15] X. Hu, Y. Shen, X. Liu, R. Fu, and J. Zi, Phys. Rev. E **69**, 030201(R) (2004).
[16] X. D. Zhang and Z. Liu, Appl. Phys. Lett. **85**, 341 (2004).
[17] P. V. Parimi, W. T. Lu, P. Vodo, and S. Sridhar, Nature (London) **426**, 404 (2003).
[18] E. Cubukcu, K. Aydin, E. Ozbay, S. Foteinopoulou, and C. M. Soukoulis, Phys. Rev. Lett. **91**, 207401 (2003).
[19] Z. Y. Li and L. L. Lin, Phys. Rev. B **68**, 245110 (2003).
[20] X. D. Zhang, Phys. Rev. B **70**, 205102 (2004).
[21] M. M. Sigalas and E. N. Economou, Europhys. Lett. **36**, 241 (1996); M. M. Sigalas, J. Appl. Phys. **84**, 3026 (1998).
[22] R. Martínez-Sala, J. Sancho, J. V. Sanchez, V. Gomez, J. Llinares, and F. Meseguer, Nature (London) **378**, 241 (1995).
[23] J. Mei, Z. Liu, J. Shi, and D. Tian, Phys. Rev. B **67**, 245107 (2003).
[24] Y. Y. Chen and Z. Ye, Phys. Rev. E **64**, 036616 (2001).
[25] J. Bravo-Abad, T. Ochiai, and J. Sanchez-Dehesa, Phys. Rev. B **67**, 115116 (2003).